

Article

Surface Daytime Net Radiation Estimation Using Artificial Neural Networks

Bo Jiang ^{1,*}, Yi Zhang ¹, Shunlin Liang ^{1,2}, Xiaotong Zhang ¹ and Zhiqiang Xiao ³

¹ State Key Laboratory of Remote Sensing Science, and College of Global Change and Earth System Science, Beijing Normal University, Beijing 100875, China;

E-Mails: zhangyi1990@foxmail.com (Y.Z.); xtngzhang@bnu.edu.cn (X.Z.)

² Department of Geographical Sciences, University of Maryland, College Park, MD 20742, USA;

E-Mail: sliang@umd.edu

³ State Key Laboratory of Remote Sensing Science, and School of Geography, Beijing Normal University, Beijing 100875, China; E-Mail: zhqxiao@bnu.edu.cn

* Author to whom correspondence should be addressed; E-Mail: bojiang@bnu.edu.cn; Tel.: +86-10-5880-9071; Fax: +86-10-5880-3002.

External Editors: Assefa Melesse and Prasad S. Thenkabail

Received: 7 July 2014; in revised form: 8 October 2014 / Accepted: 13 October 2014 /

Published: 11 November 2014

Abstract: Net all-wave surface radiation (R_n) is one of the most important fundamental parameters in various applications. However, conventional R_n measurements are difficult to collect because of the high cost and ongoing maintenance of recording instruments. Therefore, various empirical R_n estimation models have been developed. This study presents the results of two artificial neural network (ANN) models (general regression neural networks (GRNN) and Neuroet) to estimate R_n globally from multi-source data, including remotely sensed products, surface measurements, and meteorological reanalysis products. R_n estimates provided by the two ANNs were tested against *in-situ* radiation measurements obtained from 251 global sites between 1991–2010 both in global mode (all data were used to fit the models) and in conditional mode (the data were divided into four subsets and the models were fitted separately). Based on the results obtained from extensive experiments, it has been proved that the two ANNs were superior to linear-based empirical models in both global and conditional modes and that the GRNN performed better and was more stable than Neuroet. The GRNN estimates had a determination coefficient (R^2) of 0.92, a root mean square error (RMSE) of $34.27 \text{ W}\cdot\text{m}^{-2}$, and a bias of $-0.61 \text{ W}\cdot\text{m}^{-2}$ in global mode based on the

validation dataset. This study concluded that ANN methods are a potentially powerful tool for global R_n estimation.

Keywords: Net radiation; Artificial Neural Network; modeling; remotely sensed products

1. Introduction

Net all-wave surface radiation (R_n), characterizing the available radiative energy at the Earth's surface, is the difference between total upward and downward radiation. R_n drives the processes of evaporation, evapotranspiration, air and soil fluxes as well as other smaller energy-consuming processes such as photosynthesis [1,2]. R_n is a key component of surface energy balance and largely determines sensible and latent heat fluxes [3]. In agrometeorology, R_n is a parameter commonly used to estimate reference evapotranspiration and leaf wetness duration from physical models [4]. Thus, reliable spatial and temporal R_n information is required. However, directly measured R_n is available only from a very small number of standard radiometric observatories because of the expensive instruments and constant maintenance needed to guarantee that reliable measurements can be provided [5], and these in-situ measurements are unable to represent the spatial variability. Alternative methods for R_n estimation have, therefore, been developed to compensate for experimental observations.

Mathematically, R_n consists of four components:

$$\begin{aligned} R_n &= R_{ns} + R_{nl}, \\ R_{ns} &= R_{si} - R_{so} = (1 - \alpha)R_{si} \\ R_{nl} &= R_{li} - R_{lo} \end{aligned} \quad (1)$$

where R_{ns} is the net shortwave radiation, R_{nl} is the net longwave radiation ($\text{W}\cdot\text{m}^{-2}$), R_{si} is the incoming shortwave radiation ($\text{W}\cdot\text{m}^{-2}$), R_{so} is the reflected shortwave radiation ($\text{W}\cdot\text{m}^{-2}$), which is calculated by $R_{so} = \alpha * R_{si}$, α is the shortwave broadband albedo (dimensionless), R_{li} is the incoming longwave radiation ($\text{W}\cdot\text{m}^{-2}$), R_{lo} is the outgoing longwave radiation ($\text{W}\cdot\text{m}^{-2}$). If all components in Equation (1) are known, the calculation of R_n is straightforward.

Many radiation measurement towers that measure these four components to determine net radiation, but these measurements are available only at individual sites. To estimate R_n at regional and global scales, various methods have recently been developed, such as generating R_n from various satellite data [6], or from meteorological reanalysis products [7–9]. Although these reanalysis products are tempo-spatially continuous, their spatial resolutions are coarse. To date, the finest spatial resolution for a global product is only about 0.3° . It is extremely difficult to estimate R_n directly from satellite data because frequent cloud coverage can block surface information. However, satellite data can fortunately be used to estimate incoming solar radiation under all-sky conditions [10,11]. Therefore, an important research goal is to develop robust methods for estimating accurate, high tempo-spatial resolution R_n from incoming shortwave radiation or shortwave net radiation, producing estimates that are location independent and universally applicable.

In recent years, numerous methods for accurately estimating R_n have been explored and developed. Initially, R_n was estimated only from the incoming solar radiation, R_{si} [12,13]. Then surface albedo was

incorporated with claims that the fitting accuracy of models could be improved [14], but later studies found that the improvement brought mixed results [15]. Later, other models were developed by incorporating more meteorological parameters (*i.e.*, air temperature, cloud cover) and other variables (*i.e.*, relative Earth-Sun distance, land covers represented by the Normalized Difference Vegetation Index (NDVI)) and these models were evaluated by many studies [16–19]. In addition to these empirical models, physically-based models and hybrid models have also been developed. The physically-based models usually estimated R_n by calculating the individual terms in Equation (1) separately and most have focused on R_{nl} parameterization [20,21]. Some of these models focused on deriving R_n from satellite data for developing a continuous tempo-spatial regional or global R_n [22–25]. Recently, a study conducted by Jiang *et al.* [26] compared and evaluated seven popular empirical linear models and one newly developed model for R_n estimation using comprehensive global measurements. The results indicated that the linear empirical models performed well, but not well enough in all cases, and therefore the author suggested that nonlinear empirical models should be considered for R_n estimation.

Although significant progress has been made in this study area, some problems still remain. Physically based models are thought to be more accurate than the empirical models, but the calculations are usually more complex and time-consuming, especially because it is difficult to collect all the inputs. Therefore, empirical models are still the first option for practical applications. However, almost all popular empirical R_n estimation models consider only linear relationships between variables and therefore, nonlinear models should be explored. Ferreira *et al.* [27] and Geraldo-Ferreira *et al.* [28] sought to calculate R_n using artificial neural networks (ANN) and proved their applicability. However, only one ANN model was used, and the number of observations used were too small to represent different atmosphere and environmental conditions. This suggests that more work in this research area is needed. Furthermore, the utility of other sources of data (*i.e.*, model reanalysis products) in R_n estimation should be explored because poor quality or missing data are usually found in surface radiation measurements, meteorological variables, and even remotely-sensed products.

To address these issues, the primary objective of this study was to develop nonlinear R_n estimation models using two ANNs based on multi-source data. The data included remotely sensed products, meteorological reanalysis products, and site observations. Two newly developed ANN models, a general regression neural network (GRNN) [29] and Neuroet model [30], were used in this study. A GRNN has a multi-input-output architecture that is different from other ANN models whereas Neuroet includes a novel procedure to determine the model architecture. The performance of these two ANNs for R_n estimation, especially their adaptability to different conditions globally, was compared and analyzed. The advantages and disadvantages of each model were thereby determined, and a sensitivity analysis was carried out for the GRNN.

The remainder of this paper is organized as follows. Details of the ANN models and the data used in the study are provided in Section 2. Section 3 describes the analytical results. Discussions and concluding remarks are provided in Section 4.

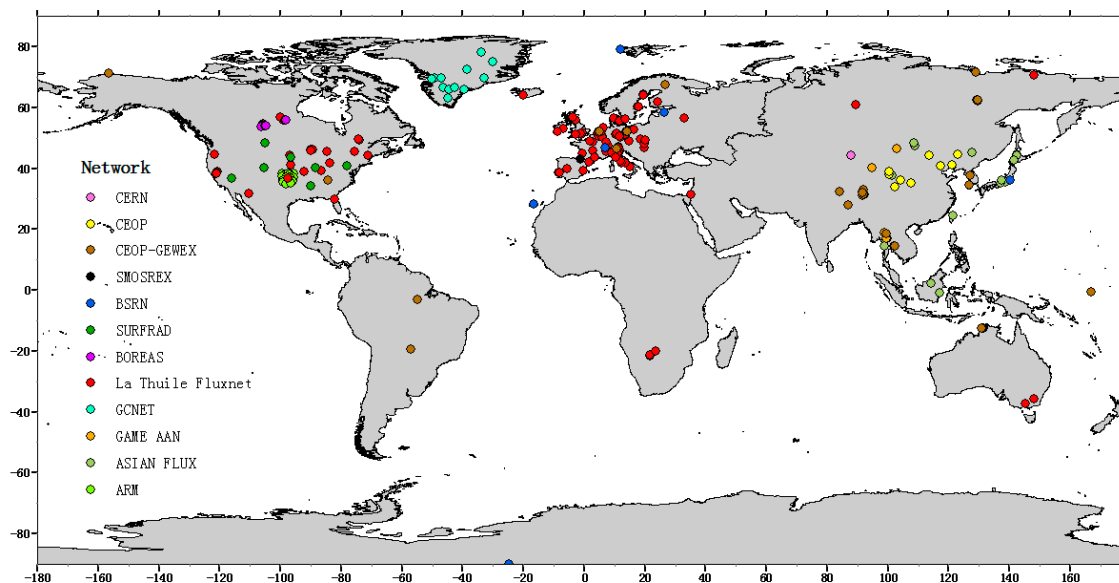
2. Data and Methodology

2.1. Data

2.1.1. In-Situ Data

Observations from 251 sites in 12 measurement networks around the world were collected as shown in Figure 1. The information collected from them and the interval of observations for each are shown in Table 1 ([31–50]). These measurements networks assured that their site observations were quality controlled, and also offered detailed information on each site. They are located across the globe and represent different climatic and ecosystem conditions ranging from the Arctic to the Antarctic. The variety of land cover types at these sites (as defined by International Geosphere-Biosphere Programme (IGBP)) is comprehensive, as indicated in Table 2. The elevation of these sites ranges from -0.7 m to 5063 m above sea level.

Figure 1 Distribution of 251 observing sites in 12 measurement networks.



To achieve a better understanding of the applicability of the two ANN models, four categories were established according to Jiang *et al.* [26]. Based on extensive experiments, Jiang *et al.* [26] found that $NDVI = 0.2$ can be used as the threshold to identify vegetated surfaces, and three more classes can be roughly divided based on albedo according to the different relations between R_{si} and R_n when $NDVI < 0.2$ as shown in Table 3. The fitting results will be discussed for each category. Though these measurements were quality controlled by the networks, they were further examined manually by us, and then all measurements were averaged to reasonable daytime values as proposed by Jiang *et al.* [26]. Note that daytime was defined as the period between sunrise and sunset at each site.

Table 1. Information related to the 12 measurement networks.

Abbreviation	Full Name	URL	Temporal Resolution
La Thuile Fluxnet	Global Fluxnet (La Thuile dataset)	[31]	30 minute
ARM	Atmospheric Radiation Measurement	[32]	10 minute
Asia Flux	\	[33]	30 minute
BSRN [34]	Baseline Surface Radiation Network	[35]	1 minute
SURFRAD [36,37]	Surface Radiation Network	[38]	3 hourly
BOREAS	Boreal Ecosystem-Atmosphere Study	[39]	30 minute
GAME AAN	GEWEX Asian Monsoon Experiment	[40]	30 minute
GC-Net [41]	Greenland Climate Network	[42]	1 hourly
CEOP-GEWEX	Coordinated Enhanced Observing Period	[43]	30 minute
CEOP [44–47]	Coordinated Enhanced Observation Network of China	\	30 minute
SMOSREX [48]	Surface Monitoring Of Soil Reservoir Experiment	[49]	30 minute
CERN	Chinese Ecosystem Research Network	[50]	30 minute

Table 2. Number of sites for each International Geosphere-Biosphere Programme (IGBP) land cover types.

IGBP Land Cover Types	No. of Sites
Barren& Sparse vegetation	6
Cropland	43
Deciduous Broadleaf Forest (DBF)	28
Deciduous Needleleaf Forest (DNF)	7
Evergreen Broadleaf Forest (EBF)	10
Evergreen Needleleaf Forest (ENF)	47
Grassland	57
Ice	18
Mixed Forest (MF)	8
Savanna	6
Shrubland	10
Wetland	11
Total	251

Table 3. Four classifications based on combinations of Normalized Difference Vegetation Index (NDVI) and albedo (remotely sensed product introduced in Section 2.1.2), with their corresponding numbers of observations.

Class	Classification Criteria	No. of Observations
S1	$NDVI < 0.2$ and $albedo \leq 0.25$	9790
S2	$NDVI < 0.2$ and $0.25 < albedo < 0.7$	9974
S3	$NDVI < 0.2$ and $albedo \geq 0.7$	8930
S4	$NDVI \geq 0.2$	173,396

2.1.2. Remotely Sensed Data

Changes in land surface can be characterized by long-term NDVI and surface albedo and, therefore, these two satellite products were used in this study. The bi-weekly, 8-km NDVI product from 1982–2010 was used, which is derived from the data of Advanced High Resolution Radiometer (AVHRR) on the National Oceanic and Atmospheric Administration (NOAA) polar-orbiting satellite by the NASA Global Inventory Monitoring and Modeling Studies (GIMMS) [51]. This dataset has been widely used. The Global Land Surface Satellite (GLASS) albedo product from 1981–2010 at 8-day temporal resolution and 0.05° spatial resolution was also used. It has been demonstrated that the GLASS albedo product is superior to most of the albedo products available today and its accuracy can satisfy various applications [52–55]. NDVI and albedo time-series data were extracted for each site.

2.1.3. Model Reanalysis Data

Reanalysis data were used for global mapping in the present study because of the limited coverage of field meteorological observation networks. The NASA Modern Era Retrospective-Analysis for Research and Applications (MERRA) [8] was used, which has been used widely in various studies. Multiple meteorological variables, including maximum air temperature (T_{max} , °C), minimum air temperature (T_{min} , °C), mean air temperature (T_a , °C), diurnal temperature (DTR , °C), wind speed (W , m·s⁻¹), and surface air pressure (PS , Pa), were first extracted for each site from 1982 to 2010, and the hourly MERRA data were then aggregated into daily values. Because relative humidity (RH , %) and water vapor pressure (e_a , kPa) could not be extracted from MERRA directly, they were calculated as in Equations (2) [56] and (3) respectively:

$$RH = \frac{PS_{pa} / ((m_{dry} qv_{kg/kg} + m_{h_2o} - m_{h_2o} qv_{kg/kg}) / (qv_{kg/kg} m_{dry}))}{a_0 + T_{a, \circ C} (a_1 + T_{a, \circ C} (a_2 + T_{a, \circ C} (a_3 + T_{a, \circ C} (a_4 + T_{a, \circ C} (a_5 + T_{a, \circ C} a_6 / 1000)))))} \quad (2)$$

where PS_{pa} is surface air pressure, and $qv_{kg/kg}$ is the specific humidity, m_{dry} and m_{h_2o} are the molar mass of dry air and water, and they were defined as 28.9644 g/mol and 18.01534 g/mol respectively. The denominator is used for vapor pressure of water calculation [57], and the constants were defined as: $a_0 = 6.107799961$, $a_1 = 0.443651$, $a_2 = 1.4289 \times 10^{-2}$, $a_3 = 2.65 \times 10^{-4}$, $a_4 = 3.03 \times 10^{-6}$, $a_5 = 2.03 \times 10^{-8}$, and $a_6 = 6.1368 \times 10^{-8}$.

$$e_a = \begin{cases} RH \times (0.6108 \times e^{\frac{22.46 T_{a, \circ C}}{T_{a, \circ C} + 272.62}}) & \text{if IGBP type is "Ice"} \\ RH \times (0.6108 \times e^{\frac{17.27 T_{a, \circ C}}{T_{a, \circ C} + 237.3}}) & \text{other IGBP types} \end{cases} \quad (3)$$

where $T_a, \circ C$ and RH were obtained from MERRA, and e_a was calculated based on whether the IGBP land cover type is ice or not.

2.1.4. Other Parameters

In addition to the data described above, certain parameters needed to be calculated. Because of the difficulty in collecting cloud data, the Clearness Index (CI) [17] and the Brightness Index (BI) were used to denote cloud information, they were calculated as follows:

$$\begin{aligned} CI &= \frac{R_{si}}{R_{se}}, \\ BI &= \frac{R_{si}}{R_{sc}} \end{aligned} \quad (4)$$

where R_{se} ($W \cdot m^{-2}$) is extraterrestrial radiation and R_{sc} ($W \cdot m^{-2}$) is clear-sky theoretical surface radiation. The calculation of these using Equation (5) shows that [58]:

$$\begin{aligned} R_{se} &= \frac{1440G_{sc}d_r}{\pi} (\omega_s \sin(\varphi) \sin(\delta) + \cos(\delta) \sin(\omega_s)) \\ d_r &= 1 + 0.033 \cos\left(\frac{2\pi DOY}{365}\right) \\ \delta &= 0.409 \sin\left(\frac{2\pi DOY}{365} - 1.39\right) \\ \omega_s &= \arccos(-\tan(\varphi) \tan(\delta)) \\ rad &= \frac{\pi}{180} * (decimal \text{ deg}) \\ R_{sc} &= (0.75 + 2 * 10^{-5} z) R_{se} \end{aligned} \quad (5)$$

where G_{sc} is the solar constant ($0.0820 \text{ MJm}^{-2} \cdot \text{min}^{-1}$), d_r is the inverse relative distance from the Earth to the Sun, ω_s is the sunset hour angle (rad), φ is the latitude (rad), δ is the solar declination (rad), z is the elevation (m), and DOY is the day of the year.

2.2. Methodology

ANNs are valuable statistical tools that can be used to approximate any complex functional relationship without pre-specifying the type of the relationship between input and response variables. Compared to conventional linear-based statistical methods, ANNs can deal with inherent data variability, provide better recognition of data patterns, and make better predictions of response variables [30]. In the present study, two newly developed ANN models, a General Regression Neural Networks (GRNN) and Neuroet, were used. Detailed information about the two models is given below:

(1) General Regression Neural Networks (GRNN)

The GRNN is a generalization of radial basis function networks and probabilistic neural networks developed by Specht *et al.* [29]. Figure 2 shows the architecture of a GRNN model used in this study. The GRNN has a multi-input-output (one output in this study) architecture, and includes four layers: input layer, pattern layer, summation layer, and output layer. The input layer provides all the variables to the neurons in the pattern layer; each neuron represents a training pattern, and its output is a measure of the distance of the input from the stored patterns. The summation layer has two types of summation

neurons: one to compute the sum of the weighted outputs of the pattern layer, and the other to calculate the unweighted outputs of the pattern neurons. Finally, the output layer performs a normalization step to yield the predicted value of the output variable. In the present study, the Gaussian kernel function was used for GRNN training, and the smoothing parameter in the kernel function was the only free parameter as Equation (6) shows:

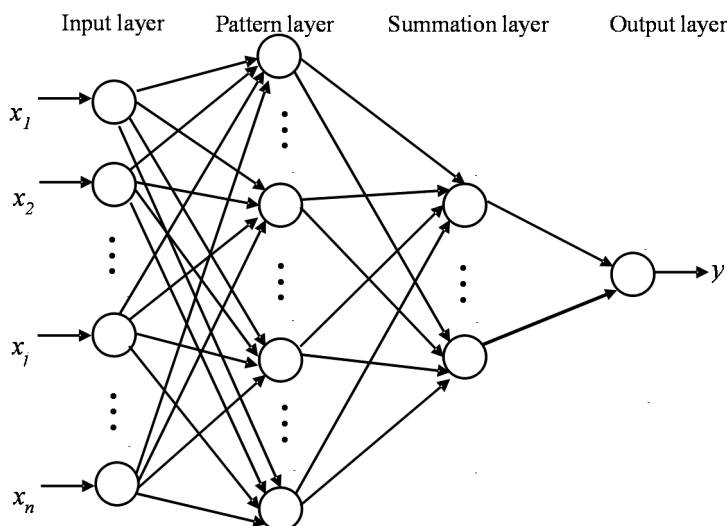
$$Y'(X) = \frac{\sum_{i=1}^n Y^i \exp(-\frac{D_i^2}{2\sigma^2})}{\sum_{i=1}^n \exp(-\frac{D_i^2}{2\sigma^2})} \tag{6}$$

where $D_i^2 = (X - X^i)^T (X - X^i)$ presents the squared Euclidean distance between the input vector X and the i th training input vector X^i , Y^i is the output vector corresponding to the vector X^i , $Y'(X)$ is the estimate corresponding to the vector X, n is the number of samples, and σ is a smoothing parameter that controls the size of the receptive region. Therefore, GRNN training was essentially optimization of the smoothing parameter, unlike back-propagation neural networks which must be iteratively trained to determine their weights, so the architecture and weights of a GRNN are determined when the input is given. The value of the smoothing parameter significantly affects the accuracy of GRNN predictions, and therefore the magnitude of the smoothing parameter must be chosen carefully. In this study, the holdout method suggested by Specht [29] was used to build the cost function (Equation (7)):

$$f(\sigma) = \frac{1}{n} \sum_{i=1}^n (\hat{Y}_i(X_i) - Y_i)^2 \tag{7}$$

where $\hat{Y}_i(X_i)$ is the estimate corresponding to X_i using the GRNN. Then the shuffled complex evolution optimization method developed by Duan [59] and Xiao *et al.* [60] was used to find the optimal smoothing parameter and used in the final GRNN. All the inputs were Z-score normalized or linearly scaled before training.

Figure2 General regression neural networks (GRNN) with multi-input-one-output architecture. The inputs $x_i (i = 1, \dots, n)$ were shown in Table 4, and the output y represents R_n .



(2) Neuroet package

Neuroet is an easy-to-use ANN package developed by Noble *et al.* [30], and is an implementation of a multi-layer perceptron neural network. This package can not only be used to train an ANN model and make predictions, but also can extract the equation defining the relationships between the input and output variables of the trained ANN and even determine the relative importance of the input variables. Moreover, the optimal number of hidden neurons, which has a non-negligible influence on ANN architecture, can be automatically determined by this package. Furthermore, the package has a user-friendly interface that guides the user to step by step train, test, and validate an ANN model. First, the number of hidden neurons should be determined to avoid over- or under-fitting the data. This, and other options associated with the ANN architecture, should be set by the user in the Preference panel. Now the ANN is ready to train and run. The importance of input variables is evaluated using the other panel in the Neuroet package. For more details, readers can refer to Noble *et al.* [30]. In the present study, the Neuroet settings for R_n estimation were: scaling method, Z-score normalization (mean = 0, standard deviation = 1) or linear scaling (maximum = 1, minimum = -1); transfer function for input neurons, log-sigmoid, and transfer function for the output neuron, pure linear; training method, Levenberg-Marquardt; and the number of hidden neurons was set according to the results. The maximum number of hidden neurons should be equal to the number of input variables.

The response and input variables used for the two ANN models are shown in Table 4.

Table 4. Summary of input and response variables.

	Abbreviation	Name	Unit	Data Type
Response Variable	R_n	Surface net radiation	$W \cdot m^{-2}$	<i>In-situ</i>
	R_{si}	Surface incoming solar radiation	$W \cdot m^{-2}$	
Independent Variables	ABD	Surface albedo		Remotely Sensed Product
	NDVI	Normalized Difference Vegetation Index		
	T	Daily air mean temperature	$^{\circ}C$	
	T_{min}	Daily air minimum temperature	$^{\circ}C$	Re-Analysis Product
	T_{max}	Daily air maximum temperature	$^{\circ}C$	
	RH	Daily mean relative humidity	%	
	PS	Surface air pressure	Pa	
	W	Wind speed	$m \cdot s^{-1}$	
	e_a	Water vapor pressure	KPa	
	d_r	Inverse relative Earth-Sun distance		
CI	Clearness Index			
BI	Brightness Index			

(3) Training and validation

For training, the whole dataset was randomly separated into two subsets: 50% for training, and the other 50% for independent validation. Because all the parameters in the GRNN can be determined automatically, the whole training dataset was used for the GRNN training. However, to obtain the

optimal model in Neuroet, the training dataset was further randomly divided in 80%, 10%, and 10% proportions for training, testing, and validation respectively, the training, testing, and validation procedures were repeated 10 times to get 10 models, and finally the optimal model in which the fitting accuracies for testing (R_t^2) and validation (R_{tt}^2) were the closest was selected as the final model. For consistency, the inputs were Z-score normalized before using the GRNN and Neuroet models.

To obtain a better understanding of the robustness of the two models, they were trained and validated against observations in two cases. In case 1, the models were trained and validated using all the observations, *i.e.*, the *global model*. In case 2, the observations were divided into several subsets based on their surface characteristics, and the models obtained were referred to as *conditional models*. In both cases, the GRNN and Neuroet models were trained according to the procedures described above.

3. Results and Discussion

The performance of these two ANN models was evaluated using the measured R_n with three measures: R^2 , root mean squared error (*RMSE*), and *bias*. The performance of the GRNN and Neuroet was first compared, followed by the results of a sensitivity analysis for the GRNN.

3.1. Comparison of the Two ANN Models

The performance of the GRNN and Neuroet as global models is shown in Table 5, and the scatter plots of the prediction and measured R_n with the two models are shown in Figure 3. The results indicate that the GRNN global model has better performance than Neuroet.

Table 5. Validation statistics for GRNN and Neuroet global models.

	Global Model		
	R^2	<i>RMSE</i> ($\text{W}\cdot\text{m}^{-2}$)	<i>bias</i> ($\text{W}\cdot\text{m}^{-2}$)
GRNN	0.92	34.27	−0.61
Neuroet	0.91	37.79	0.10

The robustness of the two models in global mode was examined by comparing the prediction accuracies of four categories, with the results shown in Table 6 and Figure 4 (Figure 4a–d, 4i–l). Generally speaking, the GRNN global model worked much better and more stable than Neuroet, especially for S2 and S3, which were difficult to represent by empirical linear models [26]. It is noteworthy that the prediction for S3 by the two models was also quite well if the RMSEs and biases were examined rather than R^2 , which indicates that all points were relatively clustered (Figure 4c,g,k,o). For S1 and S4, however, the performance of the two models was similar.

The performance of the GRNN and Neuroet in the conditional mode for these four categories was also examined and the results given in Table 6 and Figure 4 (Figure 4b,f,j,n,d,h,l,p). The regression statistics for Neuroet were significantly improved for each category, but improved only slightly for the GRNN. For example, for Neuroet, the fitting R^2 increased from 0.55 to 0.80 and the *RMSE* decreased from 51.32 to 34.69 ($\text{W}\cdot\text{m}^{-2}$) for S2, and R^2 increased from 0.22 to 0.40, *RMSE* decreased from 17.42 to 15.31 ($\text{W}\cdot\text{m}^{-2}$), and *bias* changed from −1.71 to 0.06 ($\text{W}\cdot\text{m}^{-2}$) for S3. However, for S1, R^2 increased from 0.82 to 0.89 and *RMSE* decreased from 49.06 to 37.86 ($\text{W}\cdot\text{m}^{-2}$), with little change in *bias*. On the

other hand, the fitting accuracy changed very little for the GRNN across the four categories, and the bias even increased for S1 with the conditional model. Overall, the Neuroet conditional models worked similarly to the GRNN conditional models or the global model.

Figure 3. Scatter plot of predicted and measured R_n by (a) GRNN and (b) Neuroet model in global mode.

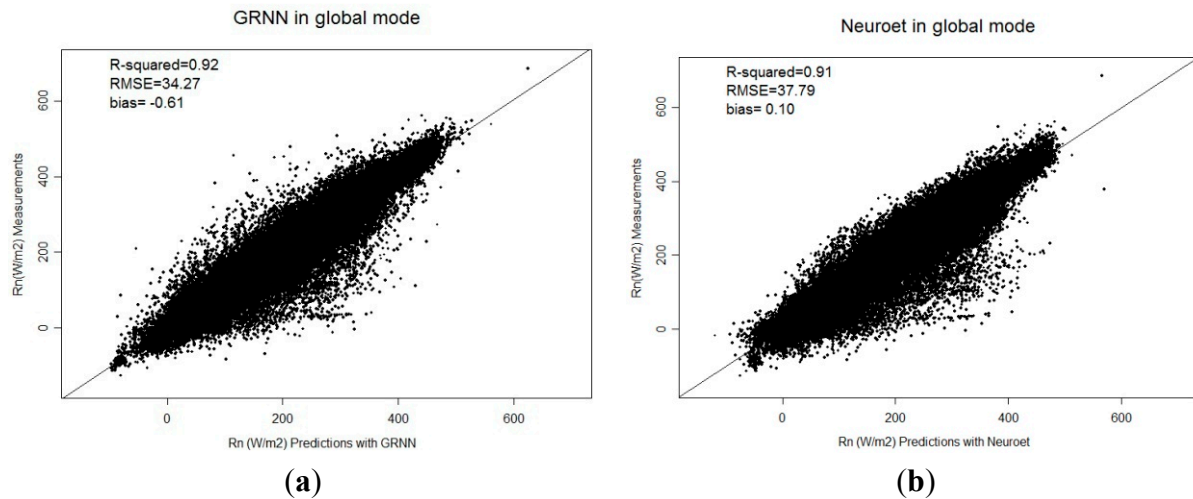


Table 6. Validation statistics for GRNN and Neuroet global and conditional models for the four categories.

Global Model								
	S1		S2		S3		S4	
	GRNN	Neuroet	GRNN	Neuroet	GRNN	Neuroet	GRNN	Neuroet
R^2	0.84	0.82	0.80	0.55	0.33	0.22	0.92	0.91
$RMSE$ ($W \cdot m^{-2}$)	46.75	49.06	34.58	51.32	16.16	17.42	34.07	36.82
bias ($W \cdot m^{-2}$)	1.49	0.16	-0.37	0.38	-0.42	-1.71	-0.75	0.18
Conditional Models								
	S1		S2		S3		S4	
	GRNN	Neuroet	GRNN	Neuroet	GRNN	Neuroet	GRNN	Neuroet
R^2	0.85	0.89	0.81	0.80	0.37	0.40	0.92	0.91
$RMSE$ ($W \cdot m^{-2}$)	44.77	37.86	33.82	34.69	15.66	15.31	33.16	36.57
bias ($W \cdot m^{-2}$)	3.30	0.47	0.45	-0.49	0.02	0.06	-0.94	0.52

As described above, only one free parameter (the smoothing parameter) needs to be determined in the GRNN, and therefore the architecture of the GRNN is relatively stable compared to Neuroet; this may be one of the main reasons for explaining the robustness of the GRNN global model. On the other hand, Table 7, which presents the optimal number of hidden neurons and the R_t^2 and R_{tt}^2 of the selected Neuroet model for each type, indicates that the Neuroet global model was not universally applicable. The optimal number of hidden neurons was the same for the global model and the S4 conditional model,

which illustrates that the structures of these two models were similar, and the comparative results also proved that the fitting accuracy remained almost unchanged for the two cases. However, the model structures differed between the global model and the S1–S3 conditional models, and therefore fitting accuracies improved greatly when using the Neuroet conditional model for S1–S3.

Figure 4. Scatter plots for (a, b, c, d) GRNN global and (e, f, g, h) conditional models for the four categories, scatter plots for (i, j, k, l) Neuroet global and (m, n, o, p) conditional models.

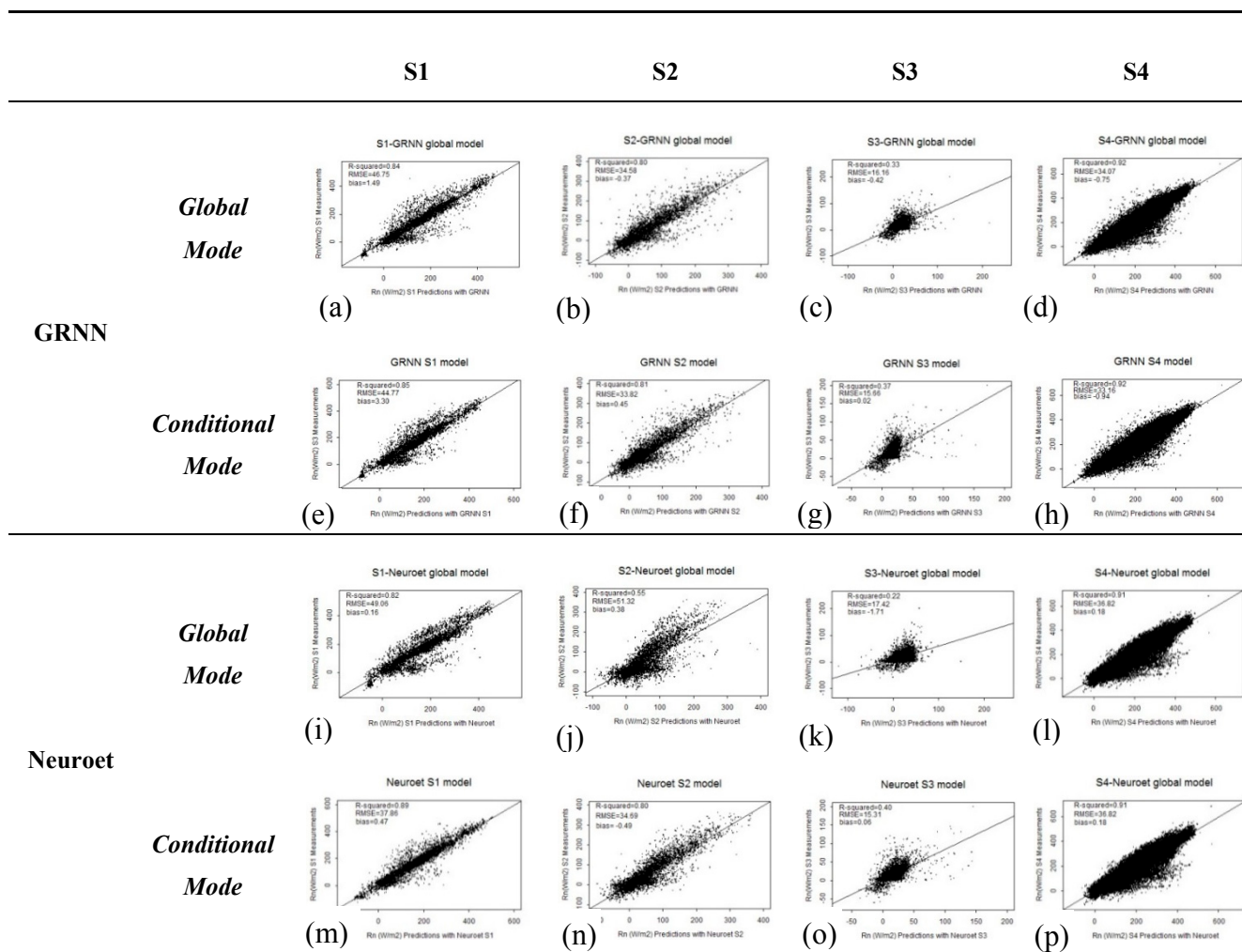


Table 7. Neuroet modeling of R_n for four categories.

Model Type	Optimal Number of Hidden Neurons	R_t^2	R_{tt}^2
Global	14	0.91	0.91
S1	13	0.93	0.89
S2	12	0.75	0.76
S3	10	0.44	0.44
S4	14	0.90	0.91

One question people may want to ask is whether the performances of these two models depend on the weather conditions. The day-time net radiation is dominated by shortwave net radiation, which is much smaller under cloudy conditions. When we examine the scatterplots in Figures 4 and 5, it is

difficult to see any significant differences in model performance between low and high values, which indicate that both models are highly robust under different weather conditions.

Based on our previous studies, it is found that the best prediction *RMSE* with linear models in global mode was still larger than $40 \text{ W}\cdot\text{m}^{-2}$, while the performances of these linear models in conditional mode were worse than GRNN and Neuroet [26]. Therefore, it can be concluded that the GRNN performs better and is more stable than the Neuroet model. Neuroet works better in the conditional mode in some specific cases than in the global mode. However, these two models were both more suitable than the linear models for R_n estimation.

3.2. Influences of Data Scaling

All variables must be scaled before using ANN models because this ensures that the values are within an appropriate range for the transfer function and is also helpful in achieving better performance and convergence. Two scaling methods are typically used in machine learning algorithms: Z-score normalization (mean = 0, standard deviation = 1) and linear scaling (maximum = 1, minimum = -1). To obtain a better understanding of the influence of scaling methods on the two models, the above procedure was repeated, but with linear scaling of the inputs for the GRNN and Neuroet models. The fitting accuracies of the two ANN models with different scaling methods for each category are compared in Table 8. It was found that the influence of scaling method was larger on the GRNN than on the Neuroet model in general and that the R^2 and *RMSE* values of the two models with the two scaling methods for each type were very close except with respect to *bias*. The values of *bias* were almost all increased when linear scaling was used in the GRNN for S1–S3, whereas the *bias* remained almost unchanged in Neuroet. These results demonstrate that the scaling method should be carefully selected in the GRNN when the sample size is small or the data values are dispersed. And also we speculated that the larger bias of GRNN in global mode (Table 5) might be caused by the scaling method due to the dispersed samples.

Table 8. Comparison of observed *versus* predicted R_n with Z-score normalization and linear scaling method for GRNN and Neuroet global and S1-S4 conditional models.

Model Type	GRNN						Neuroet					
	Z-Score Normalized			Linear Scaling			Z-Score Normalized			Linear Scaling		
	R^2	<i>RMSE</i> ($\text{W}\cdot\text{m}^{-2}$)	<i>bias</i> ($\text{W}\cdot\text{m}^{-2}$)	R^2	<i>RMSE</i> ($\text{W}\cdot\text{m}^{-2}$)	<i>bias</i> ($\text{W}\cdot\text{m}^{-2}$)	R^2	<i>RMSE</i> ($\text{W}\cdot\text{m}^{-2}$)	<i>bias</i> ($\text{W}\cdot\text{m}^{-2}$)	R^2	<i>RMSE</i> ($\text{W}\cdot\text{m}^{-2}$)	<i>bias</i> ($\text{W}\cdot\text{m}^{-2}$)
Global	0.92	34.27	-0.61	0.93	33.05	-0.29	0.91	37.79	0.10	0.91	37.67	0.61
S1	0.85	44.77	3.30	0.85	43.43	18.58	0.89	37.86	0.47	0.88	39.86	0.93
S2	0.81	33.82	0.45	0.83	31.53	30.87	0.80	34.69	-0.49	0.77	36.83	0.11
S3	0.37	15.66	0.02	0.44	14.72	7.85	0.40	15.31	0.06	0.36	15.71	-0.05
S4	0.92	33.16	-0.94	0.92	33.08	0.92	0.91	36.57	0.52	0.91	36.67	-0.49

3.3. Sensitivity Analysis

Sensitivity analysis was used to identify the input variables that contributed most to R_n estimation. Because GRNN performance was generally better than Neuroet, so the GRNN global model was taken for sensitivity analysis. The objective was to explore whether a GRNN global model developed with highly sensitive input variables could improve R_n estimation.

The typical method involved changing one input variable to its maximum and minimum values while keeping the other input variables constant (*i.e.*, at their average values) to see what effect this had on the predicted output. According to Kang *et al.* [61], the change in the output when using the minimum or maximum to average value of an input variable was also considered in addition to the conventional approach in this study. $Y^*(\text{mean})$ denotes the output variable of all input variables by their mean values, whereas $Y^*(\text{min/max})$ denotes the output variable of one input variable of interest at its minimum or maximum value. The difference in the output $Y^*(\text{min/max})$ from its mean value $Y^*(\text{mean})$ reflects how sensitive the output is to this particular input variable. The percentage relative sensitivity was calculated by the sensitivity of the input variable of interest divided by the sum of the absolute sensitivity of all input variables, that is,

$$(Y^*(\text{min/max}) - Y^*(\text{mean}))_i / \sum \text{absolute}(Y^*(\text{min/max}) - Y^*(\text{mean}))_i \quad (8)$$

where i denotes the number of input variables.

Figure 5. Sensitivity analysis of the variables used to predict R_n .

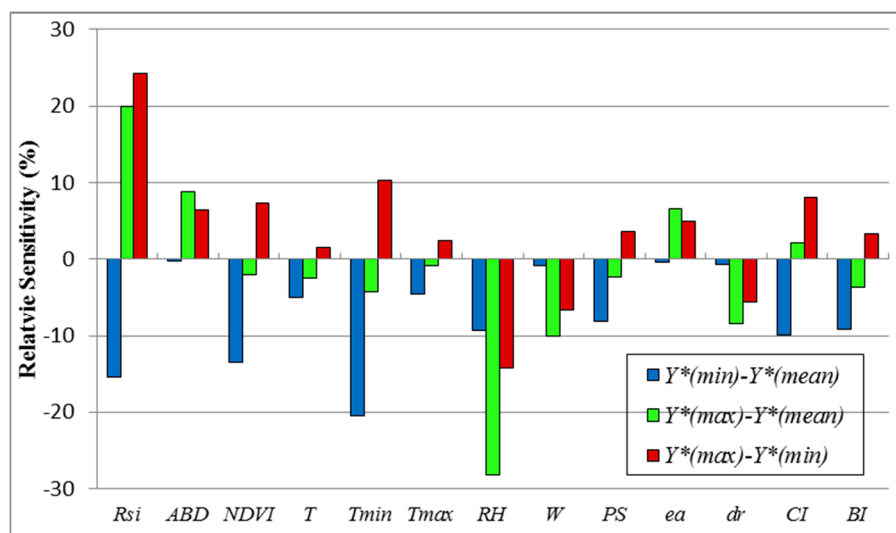


Figure 5 shows three colored bars for each input variable. The blue bars represent the change in R_n relative to minimum values of each input variable, the green bars represent the change in the R_n relative to maximum values of each input variable, and the red bars represent the change in the output variable over the entire range of values for each input variable. When the minimum to average values of the input variables were considered, the low T_{min} , low R_{si} , low $NDVI$, low CI , and low RH were found to reflect a low R_n estimate, whereas when the maximum to average values of the input variables were considered, the low RH , high R_g , low W , high ABD , low dr , and high e_a reflected a high R_n estimate. Conventional sensitivity analysis revealed less information than the analysis conducting using either minimum or

maximum input values, but it also indicated that R_{si} , RH , T_{min} , and CI were the main input variables affecting R_n .

According to the rank order obtained from Figure 5, R_{si} , $NDVI$, T_{min} , RH , and CI were before 6 in at least two sensitivity terms, so they were selected as the primary input variables. It was then found that the modeling result was the most satisfactory if ABD is added as one input after extensive experiments. Finally, the new GRNN global model with six input variables (R_{si} , ABD , $NDVI$, T_{min} , RH , and CI) was trained, validated, and compared to the original model. The validation results showed that the fitting R^2 was 0.9141, the $RMSE$ was $36.3534 \text{ W}\cdot\text{m}^{-2}$, and the $bias$ was $-0.3855 \text{ W}\cdot\text{m}^{-2}$ for the new model; these values were very similar to those from the original model (Table 4). Therefore, it has been proved that six input variables (R_{si} , ABD , $NDVI$, T_{min} , RH , and CI) are enough to fit the GRNN global model.

4. Conclusions

The high-resolution net radiation product of land surfaces is very important for many applications. Two ANN models were developed for R_n estimation using multi-source data, including remotely sensed products, reanalysis products and *in-situ* observations. To achieve a better understanding of the performance of the two models, the most comprehensive radiation ground measurements were collected for evaluation from 251 worldwide independent sites from 1992 through 2010, representing the major land cover types on Earth. The performance of the GRNN and Neuroet models was evaluated using the entire dataset (global mode) or four subsets based on surface albedo and $NDVI$ values (conditional mode). Influence of scaling methods on these two models was also discussed. The importance of each input variable for the GRNN was examined using sensitivity analysis.

Based on extensive evaluations, it was found that the GRNN performed better and more stable than Neuroet in global mode, and its estimates had the determination coefficient (R^2) of 0.92, a root mean square error ($RMSE$) of $34.27 \text{ W}\cdot\text{m}^{-2}$, and a $bias$ of $-0.61 \text{ W}\cdot\text{m}^{-2}$ based on validation. Neuroet can work as well as the GRNN in the conditional mode for four specific cases, and the GRNN conditional models performed similarly to the GRNN global model, which also proves the robustness of the GRNN model.

Furthermore, the structures of the two models can be re-built, which illustrates that the GRNN and Neuroet are not “black boxes” like other ANN models. In general, these two ANN models were found to be superior to linear regression models in terms of fitting accuracy, especially in some specific cases (*i.e.*, S2 and S3), in which the fitting $RMSE$ s were 33.82 and $15.66 \text{ W}\cdot\text{m}^{-2}$ and 34.69 and $15.31 \text{ W}\cdot\text{m}^{-2}$ by GRNN and Neuroet conditional models respectively. Experimental results indicated that the Z-score normalization method was preferable in the GRNN and Neuroet models in this study, but that highly dispersed inputs would affect GRNN performance. Sensitivity analysis of the GRNN model suggested that R_{si} , ABD , $NDVI$, T_{min} , RH , and CI were the major contributors to predictive accuracy, but the time needed for model training and prediction remained almost unchanged, which proved that the computational efficiency was determined mostly by the size of the training samples in the GRNN.

Although the GRNN has better performance than Neuroet in this study, some limitations still remain. First, the time required for GRNN model training and prediction is determined by sample size, which means that the GRNN is not suitable for a huge amount of data, whereas the time for Neuroet is shorter. Second, an under- or over-fitting problem is hard to detect in a GRNN because the entire training procedure is automatic and only the smoothing parameter can be adjusted. By contrast, the process of

determining the optimal hidden number of neurons and other key parameters in Neuroet can be helpful in obtaining the optimal model. Third, the importance of each independent variable can be easily obtained from Neuroet, but not in GRNN. In summary, although GRNN and Neuroet each had their own advantages and shortcomings, both work well for R_n estimation compared to linear regression models and therefore, both could potentially be highly useful tools for future R_n estimation.

In the future, additional efforts should be pursued to improve the optimization methods for smoothing parameter determination in the GRNN that are essential to shortening the running time.

Acknowledgments

This study was funded by the National High-Technology Research and Development Program of China under Grant 2013AA122800, the Natural Science Foundation of China (No. 41401381, No. 41101310, and No. 41331173), the Fundamental Research Funds for the Central Universities under Grant 2013NT28, and the International S&T Cooperation Program of China under Grant 2012DFG21710. This work used eddy covariance data acquired by the FLUXNET community and in particular by the following networks: AmeriFlux (U.S. Department of Energy, Biological and Environmental Research, Terrestrial Carbon Program (DE-FG02-04ER63917)), AfriFlux, AsiaFlux, CarboAfrica, CarboEuropeIP, CarboItaly, CarboMont, ChinaFlux, Fluxnet-Canada (supported by CFCAS, NSERC, BIOCAP, Environment Canada, and NRCan), GreenGrass, KoFlux, LBA, NECC, OzFlux, TCOS-Siberia, and USCCC. We acknowledge the financial support to the eddy covariance data harmonization provided by CarboEuropeIP, FAO-GTOS-TCO, Ileaps, Max Planck Institute for Biogeochemistry, National Science Foundation, University of Tuscia, Université Laval, Environment Canada and the U.S. Department of Energy and the datasets development and technical support from Berkeley Water Center, Lawrence Berkeley National Laboratory, Microsoft Research eScience, Oak Ridge National Laboratory, University of California—Berkeley and the University of Virginia. We also would like to thank Yan Li and Ran Li from the Xinjiang Institute of Ecology and Geography, CAS, and Jean Christophe Calvet from CNRM-GAME for sharing their data. Finally, we would like to thank Peter A. Noble from the University of Washington, USA, for providing the Neuroet software and valuable suggestions. Besides, the authors would like to thank the anonymous reviewers for their valuable suggestions and comments.

Author Contributions

Bo Jiang designed this study, performed the experiments and wrote the main part of the manuscript. The co-authors of this manuscript significantly contributed to all phases of the investigation: Shunlin Liang supervised this research and contributed to the research design and manuscript writing. Yi Zhang contributed to the data analyses and part of the experiments. Xiaotong Zhang and Zhiqiang Xiao contributed to the model implementation and data analyses.

Conflicts of Interest

The authors declare no conflict of interest.

References

1. Rosenberg, N.J.; Blad, B.L.; Verma, S.B. *Microclimate—The Biological Environment*; Wiley: New York, NY, USA, 1983; pp. 44–45.
2. Hurtado, E.; Sobrino, J.A. Daily net radiation estimated from air temperature and NOAA-AVHRR data: A case study for the Iberian Peninsula. *Int. J. Remote Sens.* **2001**, *22*, 1521–1533.
3. Kalthoff, N.; Fiebig-Wittmaack, M.; Meibner, C.; Kohler, M.; Uriarte, M.; Bischoff-Gauß, I.; Gonzales, E. The energy balance, evapotranspiration and nocturnal dew deposition of an arid valley in the andes. *J. Arid Environ.* **2006**, *65*, 420–443.
4. Allen, R.; Tasumi, M.; Trezza, R. Satellite-based energy balance for mapping evapotranspiration with internalized calibration (metric)—Model. *J. Irrig. Drain. Eng.* **2007**, *133*, 380–394.
5. Monteith, J.L.; Unsworth, M.H. *Principles of Environmental Physics*; Edward Arnold: London, UK, 1990; p. 291.
6. Liang, S.L.; Wang, K.C.; Zhang, X.T.; Wild, M. Review on estimation of land surface radiation and energy budgets from ground measurement, remote sensing and model simulations. *IEEE J. Sel. Top. Appl. Earth Obs. Remote Sens.* **2010**, *3*, 225–240.
7. Dee, D.P.; Uppala, S.M.; Simmons, A.J.; Berrisford, P.; Poli, P.; Kobayashi, S.; Andrae, U.; Balmaseda, M.A.; Balsamo, G.; Bauer, P.; *et al.* The era-interim reanalysis: Configuration and performance of the data assimilation system. *Q. J. R. Meteorol. Soc.* **2011**, *137*, 553–597.
8. Rienecker, M.M.; Suarez, M.J.; Gelaro, R.; Todling, R.; Bacmeister, J.; Liu, E.; Bosilovich, M.G.; Schubert, S.D.; Takacs, L.; Kim, G.K.; *et al.* Merra: Nasa’s modern-era retrospective analysis for research and applications. *J. Clim.* **2011**, *24*, 3624–3648.
9. Uppala, S.M.; Kållberg, P.W.; Simmons, A.J.; Andrae, U.; Bechtold, V.D.C.; Fiorino, M.; Gibson, J.K.; Haseler, J.; Hernandez, A.; Kelly, G.A.; *et al.* The era-40 re-analysis. *Q. J. R. Meteorol. Soc.* **2005**, *131*, 2961–3012.
10. Liang, S.L.; Zhang, X.T.; He, T.; Cheng, J.; Wang, D.D. Remote sensing of Earth surface radiation budget. In *Remote Sensing of Land Surface Turbulent Fluxes and Soil Surface Moisture Content: State of the Art*; Petropoulos, G.P., Ed.; CRC Press: Boca Raton, FL, USA, 2013; pp. 125–165.
11. Zhang, X.T.; Liang, S.L.; Q., Z.G.; Wu, H.R.; Zhao, X. Generating Global Land Surface Satellite (GLASS) incident shortwave radiation and photosynthetically active radiation products from multiple satellite data. *Remote Sens. Environ.* **2014**, *152*, 318–332.
12. Davies, J.A. A note on relationship between net radiation and solar radiation. *Q. J. R. Meteorol. Soc.* **1967**, *93*, 109–115.
13. Gay, L. The regression of net radiation upon solar radiation. *Theor. Appl. Climatol.* **1971**, *19*, 1–14.
14. Kaminsky, K.Z.; Dubayah, R. Estimation of surface net radiation in the boreal forest and northern prairie from shortwave flux measurements. *J. Geophys. Res. Atmos.* **1997**, *102*, 29707–29716.
15. Alados, I.; Foyo-Moreno, I.; Olmo, F.J.; Alados-Arboledas, L. Relationship between net radiation and solar radiation for semi-arid shrub-land. *Agric. For. Meteorol.* **2003**, *116*, 221–227.
16. Al-Riahi, M.; Al-Jumaily, K.; Kamies, I. Measurements of net radiation and its components in semi-arid climate of baghdad. *Energy Convers. Manag.* **2003**, *44*, 509–525.

17. Iziomon, M.G.; Mayer, H.; Matzarakis, A. Empirical models for estimating net radiative flux: A case study for three mid-latitude sites with orographic variability. *Astrophys. Space Sci.* **2000**, *273*, 313–330.
18. Kjaersgaard, J.; Cuenca, R.; Plauborg, F.; Hansen, S. Long-term comparisons of net radiation calculation schemes. *Bound. Layer Meteorol.* **2007**, *123*, 417–431.
19. Wang, K.; Liang, S. Estimation of daytime net radiation from shortwave radiation measurements and meteorological observations. *J. Appl. Meteorol. Climatol.* **2009**, *48*, 634–643.
20. Kjaersgaard, J.H.; Cuenca, R.H.; Martinez-Cob, A.; Gavilan, P.; Plauborg, F.; Mollerup, M.; Hansen, S. Comparison of the performance of net radiation calculation models. *Theor. Appl. Climatol.* **2009**, *98*, 57–66.
21. Sentelhas, P.C.; Gillespie, T.J. Estimating hourly net radiation for leaf wetness duration using the penman-monteith equation. *Theor. Appl. Climatol.* **2008**, *91*, 205–215.
22. Bisht, G.; Bras, R.L. Estimation of net radiation from the MODIS data under all sky conditions: Southern great plains case study. *Remote Sens. Environ.* **2010**, *114*, 1522–1534.
23. Bisht, G.; Venturini, V.; Islam, S.; Jiang, L. Estimation of the net radiation using modis (moderate resolution imaging spectroradiometer) data for clear sky days. *Remote Sens. Environ.* **2005**, *97*, 52–67.
24. Long, D.; Gao, Y.; Singh, V.P. Estimation of daily average net radiation from modis data and dem over the Baiyangdian watershed in north China for clear sky days. *J. Hydrol.* **2010**, *388*, 217–233.
25. Ma, Y.; Su, Z.; Li, Z.; Koike, T.; Menenti, M. Determination of regional net radiation and soil heat flux over a heterogeneous landscape of the Tibetan plateau. *Hydrol. Process.* **2002**, *16*, 2963–2971.
26. Jiang, B.; Zhang, Y.; Liang, S.L.; Yao, Y.J.; Jia, K.; Zhao, D. Empirical estimation of daytime net radiation from shortwave radiation and the other ancillary information. *Agric. For. Meteorol.* **2014**, under review.
27. Ferreira, A.; Soria-Olivas, E.; López, A.; Lopez-Baeza, E. Estimating net radiation at surface using artificial neural networks: A new approach. *Theor. Appl. Climatol.* **2011**, *106*, 263–279.
28. Geraldo-Ferreira, A.; Soria-Olivas, E.; Gomez-Sanchis, J.; Serrano-Lopez, A.J.; Velazquez-Blazquez, A.; Lopez-Baeza, E. Modelling net radiation at surface using “in situ” netpyrradiometer measurements with artificial neural networks. *Expert Syst. Appl.* **2011**, *38*, 14190–14195.
29. Specht, D.F. A general regression network. *IEEE Trans. Neural Netw.* **1991**, *2*, 568–576.
30. Noble, P.A.; Tribou, E.H. Neuroet: An easy-to-use artificial neural network for ecological and biological modeling. *Ecol. Model.* **2007**, *203*, 87–98.
31. Fluxnet. Available online: <http://www.fluxdata.org/> (accessed on 7 November 2014).
32. U.S. Department of Energy. ARM-Data. Available online: <http://www.archive.arm.gov/> (accessed on 7 November 2014).
33. AsiaFlux. Available online: <http://www.asiaflux.net/> (accessed on 7 November 2014).
34. Ohmura, A.; Gilgen, H.; Hegner, H.; Müller, G.; Wild, M.; Dutton, E.G.; Forgan, B.; Fröhlich, C.; Philipona, R.; Heimo, A.; *et al.* Baseline Surface Radiation Network (BSRN/WCRP): New precision radiometry for climate research. *Bull. Am. Meteorol. Soc.* **1998**, *79*, 2115–2136.
35. BSRN-World Radiation Monitoring Center Baseline Surface Radiation Network. Available online: <http://www.bsrn.awi.de/> (accessed on 7 November 2014).

36. Augustine, J.A.; DeLuisi, J.J.; Long, C.N. SurfRad—A national surface radiation budget network for atmospheric research. *Bull. Am. Meteorol. Soc.* **2000**, *81*, 2341–2357.
37. Augustine, J.A.; Hodges, G.B.; Cornwall, C.R.; Michalsky, J.J.; Medina, C.I. An update on SURFRAD—The GCOS surface radiation budget network for the continental United States. *J. Atmos. Ocean. Technol.* **2005**, *22*, 1460–1472.
38. ESRL Global Monitoring Division. Available online: <http://www.esrl.noaa.gov/gmd/grad/surfrad/> (accessed on 7 November 2014).
39. BOREAS Project. Available online: http://daac.ornl.gov/BOREAS/bhs/BOREAS_Home.html (accessed on 7 November 2014).
40. GAME-AAN. Available online: <http://www.hyarc.nagoya-u.ac.jp/game/phase-1/game-aan.html> (accessed on 7 November 2014).
41. Steffen, K.; Box, J.; Abdalati, W. Greenland climate network: GC-Net. In *US Army Cold Regions Reattach and Engineering (CRREL); CRREL Special Report*; University of Colorado at Boulder: Boulder, CO, USA, 1996; pp. 98–103.
42. Greenland Climate Network (GC-Net). Available online: <http://cires.colorado.edu/science/groups/steffen/gcnet/> (accessed on 7 November 2014).
43. Earth Observing Laboratory. Available online: <http://www.eol.ucar.edu/projects/ceop/> (accessed on 7 November 2014).
44. Jia, Z.Z.; Liu, S.M.; Xu, Z.W.; Chen, Y.J.; Zhu, M.J. Validation of remotely sensed evapotranspiration over the Hai River Basin, China. *J. Geophys. Res. Atmos.* **2012**, *117*, doi:10.1029/2011JD017037.
45. Liu, S.M.; Xu, Z.W.; Wang, W.Z.; Jia, Z.Z.; Zhu, M.J.; Bai, J.; Wang, J.M. A comparison of eddy-covariance and large aperture scintillometer measurements with respect to the energy balance closure problem. *Hydrol. Earth Syst. Sci.* **2011**, *15*, 1291–1306.
46. Liu, S.M.; Xu, Z.W.; Zhu, Z.L.; Jia, Z.Z.; Zhu, M.J. Measurements of evapotranspiration from eddy-covariance systems and large aperture scintillometers in the Hai River Basin, China. *J. Hydrol.* **2013**, *487*, 24–38.
47. Xu, Z.W.; Liu, S.M.; Li, X.; Shi, S.J.; Wang, J.M.; Zhu, Z.L.; Xu, T.R.; Wang, W.Z.; Ma, M.G. Intercomparison of surface energy flux measurement systems used during the hiwater-musoexe. *J. Geophys. Res. Atmos.* **2013**, *118*, 13140–13157.
48. De Rosnay, P.; Calvet, J.C.; Kerr, Y.; Wigneron, J.P.; Lemaître, F.; Escorihuela, M.J.; Sabater, J.M.; Saleh, K.; Barrié, J.; Bouhours, G. Smosrex: A long term field campaign experiment for soil moisture and land surface processes remote sensing. *Remote Sens. Environ.* **2006**, *102*, 377–389.
49. Centre d'Etudes Spatiales de la BIOSphère. Available online: <http://www.cesbio.ups-tlse.fr/> (accessed on 7 November 2014).
50. CERN. Available online: <http://www.cerndata.ac.cn/> (accessed on 7 November 2014).
51. Tucker, C.J.; Pinzon, J.E.; Brown, M.E.; Slayback, D.A.; Pak, E.W.; Mahoney, R.; Vermote, E.F.; El Saleous, N. An extended AVHRR 8-km NDVI dataset compatible with MODIS and SPOT vegetation NDVI data. *Int. J. Remote Sens.* **2005**, *26*, 4485–4498.
52. Liang, S.; Zhao, X.; Liu, S.; Yuan, W.; Cheng, X.; Xiao, Z.; Zhang, X.; Liu, Q.; Cheng, J.; Tang, H.; *et al.* A long-term global land surface satellite (glass) data-set for environmental studies. *Int. J. Digit. Earth* **2013**, *6*, 5–33.

53. Liang, S.L.; Zhang, X.T.; Xiao, Z.Q.; Cheng, J.; Liu, Q.; Zhao, X. *Global Land Surface Satellite (Glass) Products: Algorithms, Validation and Analysis*; Springer: New York, NY, USA, 2013.
54. Liu, Q.; Wang, L.Z.; Qu, Y.; Liu, N.F.; Liu, S.H.; Tang, H.R.; Liang, S.L. Preliminary evaluation of the long-term glass albedo product. *Int. J. Digit. Earth* **2013**, *6*, 69–95.
55. Qu, Y.; Liu, Q.; Liang, S.; Wang, L.; Liu, N.; Liu, S. Improved mapping daily land-surface broadband albedo from MODIS data. *IEEE Geosci. Remote Sens. Lett.* **2014**, *52*, 907–919.
56. Air Humidity Converter. Available online: <http://www.cactus2000.de/uk/unit/masshum.shtml> (accessed on 7 November 2014).
57. Lowe, P.R.; Ficke, J.M. *The Computation of Saturation Vapor Pressure*; Environmental Prediction Research Facility, Naval Postgraduate School: Monterey, CA, USA, 1974.
58. Irmak, S.; Irmak, A.; Jones, J.; Howell, T.; Jacobs, J.; Allen, R.; Hoogenboom, G. Predicting daily net radiation using minimum climatological data. *J. Irrig. Drain. Eng.* **2003**, *129*, 256–269.
59. Duan, Q.Y.; Sorooshian, S.; Gupta, V. Effective and efficient global optimization for conceptual rainfall-runoff models. *Water Resour. Res.* **1992**, *28*, 1015–1031.
60. Xiao, Z.Q.; Liang, S.L.; Wang, J.D.; Chen, P.; Yin, X.J.; Zhang, Z.Q.; Song, J.L. Use of general regression neural networks for generating the glass leaf area index product from time-series MODIS surface reflectance. *IEEE Trans. Geosci. Remote Sens.* **2014**, *52*, 209–223.
61. Kang, H.Y.; Rule, R.A.; Noble, P.A. Artificial neural network modeling of phytoplankton blooms and its application to sampling sites within the same estuary. In *Treatise on Coastal and Estuarine Science*; Wolanski, M., Ed.; Elsevier: Amsterdam, The Netherlands, 2012; Volume 9, pp. 161–171.

© 2014 by the authors; licensee MDPI, Basel, Switzerland. This article is an open access article distributed under the terms and conditions of the Creative Commons Attribution license (<http://creativecommons.org/licenses/by/4.0/>).